Determination of accurate solar wind electron parameters using particle detectors and radio wave receivers

C. Salem,[1,2] J.-M. Bosqued,[3] D. E. Larson,[4] A. Mangeney,[1] M. Maksimovic,[1] C. Perche,[1] R. P. Lin,[4] and J.-L. Bougeret[1]

Abstract. We present a new, simple, and semiempirical method for determining accurate solar wind electron macroscopic parameters from the raw electron moments obtained from measured electron distribution functions. In the solar wind these measurements are affected by (1) photoelectrons produced by the spacecraft illumination, (2) spacecraft charging, and (3) the incomplete sampling of the electron distribution due to a nonzero low-energy threshold of the energy sweeping in the electron spectrometer. Correcting fully for these effects is difficult, especially without the help of data from other experiments that can be taken as a reference. We take here advantage of the fact that high-resolution solar wind electron parameters are obtained on board Wind using two different instruments: the electron electrostatic analyzer of the three-dimensional Plasma experiment (3DP), which provides 3-D electron velocity distribution functions every 99 s as well as 3-s resolution computed onboard moments, and the thermal noise receiver (TNR), which yields unbiased electron density and temperature every 4.5 s from the spectroscopy of the quasi-thermal noise around the electron plasma frequency. The present correction method is based on a simplified model evaluating the electron density and temperature as measured by the electron spectrometer, by taking into account both the spacecraft charging and the low-energy cutoff effects: approximating the solar wind electron distributions by an isotropic Maxwellian, we derive simple analytical relations for the measured electron moments as functions of the real ones. These relations reproduce the qualitative behavior of the variation of the raw 3DP electron density and temperature as a function of the TNR ones. In order to set up a precise "scalar correction" of the raw 3DP electron moments, we use the TNR densities and temperatures as good estimates of the real ones; the coefficients appearing in the analytical relations are obtained by a best fit to the data from both instruments during a limited period of time, chosen as a reference. This set of coefficients is then used as long as the mode of operation of the electron spectrometer is unchanged. We show that this simple scalar correction of the electron density and temperature is reliable and can be applied routinely to the high-resolution 3DP low-order moments. As a by-product, an estimate of the spacecraft potential is obtained. The odd-order moments of the distribution function (electron bulk speed and heat flux) cannot be corrected by the model since the distribution is assumed to be an isotropic Maxwellian. We show, however, that a better estimate of the electron heat flux can be obtained by replacing the electron velocity by the proton velocity.

1. Introduction

Accurate measurements of the solar wind electron density and temperature are key elements in understanding the properties and the physics of the solar wind. Usually these quantities are obtained as mo-

[1]Département de Recherche Spatiale, Observatoire de Paris-meudon, Meudon, France.

[2]Now at Space Sciences Laboratory, University of California, Berkeley, California.

[3]Centre d'Etude Spatiale des Rayonnements, Université Paul Sabatier, Toulouse, France.

[4]Space Sciences Laboratory, University of California, Berkeley, California.

ments of the measured electron velocity distribution functions (VDFs), obtained from electrostatic particle analyzers [see, e.g., *Montgomery et al.*, 1968; *Feldman et al.*, 1975; *Rosenbauer et al.*, 1977]. Typical modern instruments have the capability to provide detailed three-dimensional measurements with high time resolution, generally combining electrostatic analyzers and particle detectors (channel electron multipliers (CEMs), microchannel plates (MCPs), etc) [*Fazakerley et al.*, 1998, and references therein]. In one spacecraft spin period, such instruments scan the full sphere and provide three-dimensional (3-D) distributions over an energy range sufficiently large that the moments (density, velocity, temperature, etc) can, in principle, be easily extracted with an accuracy that depends on limitations in the measurements (see *Paschmann et al.* [1998] for details).

However, the VDF in the vicinity of the spacecraft

(S/C) is severely polluted, at low energies, by photo-electrons emitted by the S/C body, and distorted by the electric field created by the S/C charging, an electric field which modifies both the energies and direction of motion of the solar wind electrons incident on the detector.

Accurate measurements of the solar wind electron density and temperature require therefore a full correction of these two effects. Correcting for the photoelectrons is relatively straightforward. Since the photoelectrons have a typical temperature of the order of only a few eV, the disturbances caused by this population concern only the low-energy range $E \leq E_{ph} \sim 2-3$ eV and can generally be removed by considering only the energy channels above some minimal energy $E_{min} \geq E_{ph}$. However, this low-energy cutoff introduces a bias in the calculation of the electron VDF moments. This effect was studied, for instance, by *Song et al.* [1997], who developed analytical tools for correcting the moments, in many plasma conditions, neglecting the effect of the spacecraft potential.

Correcting for the S/C electric potential is much more delicate, since this potential depends itself on the values of the density and temperature that one wishes to measure. Spacecraft charging has been studied for a long time [e.g., *Grard*, 1973; *Garrett*, 1981; *Whipple*, 1981; *Goertz*, 1989], and basically two methods have been used to determine the spacecraft potential. It can be determined from inflections in the shape of the measured VDF at the energy E_{ph} separating the domains of phase space where photoelectrons are dominant from those where solar wind particles are dominant [see, e.g., *Feldman et al.*, 1975; *Phillips et al.*, 1993]; it can also be obtained by solving a set of equations expressing the fact that, far from the spacecraft, the plasma is electrically neutral and roughly time stationary, so that the corrected electron number and/or current densities are in reasonable agreement with the respective ion (protons plus alpha particles) parameters [see, e.g., *Scudder et al.*, 1981; *Pilipp et al.*, 1987]. For each of these techniques the proposed corrections are usually "scalar corrections"; that is, only particle energy changes in the electric potential are taken into account, neglecting modifications in the particle trajectories. A more sophisticated "vector correction" method [*Scime et al.*, 1994a] has also been developed, in which both the energy and the direction of motion of the electrons are corrected; this correction was applied to the electron distribution function measurements on board Ulysses.

Of these two methods of dealing with the S/C potential, the second is probably the most robust, since the energies of the solar wind ions are significantly larger than the S/C potential, so that they are almost unaffected by the S/C potential. Nevertheless, this method has also its limits. First, the solar wind alpha particle density is not always available [*Pilipp et al.*, 1987]. Second, possible temporal variations of the ion

instrument internal calibrations can lead to systematic discrepancies between ion density measurements taken from different analyzers [*Russell and Petrinec*, 1992; *Petrinec and Russell*, 1993; *Paularena and Lazarus*, 1994; *Petrinec and Russell*, 1994].

As an alternative to the use of the solar wind ion density as a reference, *Maksimovic et al.* [1998] proposed using the solar wind electron density obtained from the spectroscopy of the quasi-thermal noise (QTN) around the electron plasma frequency, which allows in-situ diagnostics of space plasmas [*Meyer-Vernet et al.*, 1998] by analyzing the spectrum of the thermal noise induced in an electric antenna by the random motion of the ambient electrons and protons. This method yields an accurate determination of the low-order moments of the electron VDFs such as the total density and bulk temperature [*Meyer-Vernet and Perche*, 1989; and references therein] which is almost insensitive to the S/C potential and photoelectron perturbations, since the volume sensed by the antenna is much larger than the spacecraft volume [*Meyer-Vernet et al.*, 1998]. We emphasize the fact that QTN spectroscopy measures the solar wind density with an accuracy of a few percent and has been extensively used on the Ulysses S/C, using data from the Unified Radio and Plasma Wave experiment (URAP) [*Stone et al.*, 1992], in the ecliptic plane at various heliocentric distances [*Maksimovic et al.*, 1995] as well as at higher latitudes [*Issautier et al.*, 1998].

The Wind spacecraft, launched November 1, 1994, was designed to observe the solar wind approaching Earth from a position near the Lagrangian point L1. Wind is equipped with radio wave receivers as part of the WAVES experiment [*Bougeret et al.*, 1995] and with particle detectors for the 3-D Plasma (3DP) experiment [*Lin et al.*, 1995] or the Solar Wind Experiment (SWE) [*Ogilvie et al.*, 1995], providing, for the first time in the solar wind, high time resolution data (4.5 s for the radio wave receiver, down to 3 s for the particle detectors). In the *Maksimovic et al.* [1998] study the WAVES and the SWE experiments have been used to make a solar wind density intercomparison, in order to correct the density measured by the SWE electron analyzer. These corrections were based on a rough estimation of the Wind S/C potential, for a short period of time. The aim of the present paper is to resume this kind of comparison in a much more detailed way by taking fully into account the effects of both the low-energy cutoff and S/C charging. More precisely, we make a comparative analysis of high-resolution solar wind electron densities simultaneously obtained by the thermal noise receiver (TNR), part of the WAVES package [*Bougeret et al.*, 1995], and by one of the pair of electron electrostatic analyzers (EESA), EESA Low, part of the 3DP experiment [*Lin et al.*, 1995] on board Wind (section 2). The 3DP experiment is able to sample a full 3-D electron VDF every 3 s. Because of the allowed telemetry rate, only the electron VDF moments, up to the heat flux,

processed on board are transmitted routinely every 3 s, while the full 3-D VDFs are transmitted only every 99 s (when Wind is in the solar wind). These 3-s resolution electron VDF moments are the highest time resolution electron moments ever obtained in the solar wind. Their use can potentially yield to very interesting study, for instance, of solar wind turbulence. However, since the onboard processing of the moments completely neglects the photoelectrons and charging effects, they must be used with caution.

Taking the TNR electron density as a reference, we first analyze qualitatively the differences between the TNR and the 3DP densities (section 3) and then fully discuss the corrections that have to be applied to the 3-s resolution 3DP data. For that we develop (section 4) a scalar correction model for the electron moments as measured by an electron spectrometer, taking into account both the spacecraft charging and the low-energy cutoff effects, but neglecting any other instrumental effects inherent to particle detectors (such as saturation, etc). The main interest of this very simple model, valid in the solar wind conditions, is to provide analytical relations between the real electron moments and the measured one. We then test the validity of these corrections (section 5) by comparing the TNR electron density and temperatures, assumed to represent the actual electron moments, to the corresponding corrected 3DP moments, for different periods of time and different low-energy thresholds E_{min}. An estimate of the spacecraft potential is also derived. We finally analyze the third-order electron moment, i.e., the electron heat flux, and show how to get a better estimation of it (section 6).

2. Experiments and Measured Solar Wind Parameters

2.1. Wind Thermal Noise Receiver

The WAVES/TNR [Bougeret et al., 1995] instrument was mainly designed to measure the thermal electric noise (TN) in the solar wind, around the electron plasma frequency f_p. Two multichannel receivers cover the frequency range of 4 to 256 kHz in five overlapping, logarithmically spaced frequency bands (A, B, C, D, and E). Each of these bands is divided into either 32 or 16 logarithmically spaced channels. For most of the time the TNR measures the thermal noise spectrum in the so-called ACE mode, i.e., with 96 channels, in three nonoverlapping frequency bands (A, C, and E), with a time resolution of 4.5 s. The determination of the electron density, $N_{e\,TNR}$, relies basically on the identification of the "plasma line" at the local electron plasma frequency, in the spectrum of the thermal noise. Then f_p is obtained, in most cases, with an accuracy of about half a frequency channel, except when the line is located at a band boundary (for example, between the A and C bands or the C and E bands); since the electron density $N_e \propto f_p^2$, half a frequency channel corresponds to

a relative uncertainty in N_e of 4.4%. Note that the total bandwidth of the TNR corresponds to an electron density range from < 1 to 500 cm^{-3}. The identification of the plasma line can be done routinely, with the neural network developed by the WAVES team at the Meudon Observatory [Richaume, 1996]. It is important to note that the neural network uses only the form of the plasma line in the noise spectrum so that the TNR electron density is obtained independently of any model for the electron distribution.

A more refined but model-dependent way to use QTN spectroscopy is to fit the data points to the theoretical power spectrum of the voltage measured at the terminals of the wire antenna, at frequencies much above the ion characteristic frequencies and the electron gyrofrequency [Meyer-Vernet and Perche, 1989; see also Meyer-Vernet et al., 1998; Issautier et al., 1999]. This method allows for the determination of the electron temperature, the electron density, and the electron bulk speed. Since the theoretical spectrum depends directly on the electron velocity distribution function $f(\mathbf{v})$ [Meyer-Vernet and Perche, 1989], one has to use a model for the electron VDF $f(\mathbf{v})$, usually the sum of two isotropic Maxwellian distributions, a core (density N_c, temperature T_c) and a halo (density N_h, temperature T_h). This model for the electron VDF has shown to be a good approximation for the observed electron distribution in the solar wind [e.g., Feldman et al., 1975; Pilipp et al., 1987]. The parameters ($N_c + N_h$, T_c, $\alpha = N_h/N_c$, and $\tau = T_h/T_c$) of the model are determined from the best fit of the model spectrum to the measured one.

It is worth noting that with this method, the determination of the electron density (obtained now to better than 3%) is independent of the model of $f(\mathbf{v})$ chosen to characterize the solar wind electrons, while the core temperature T_c is quite insensitive to the shape of the hot population distribution. Indeed, Chateau and Meyer-Vernet [1991] have shown that only the suprathermal parameters (N_h and T_h) are changed for different models of the electron distribution (for example, bi-Maxwellian or kappa distributions). For high-speed flows the ion contribution to the thermal noise cannot be neglected anymore because it is Doppler shifted to higher frequencies and hence affects significantly the electron QTN. The QTN method has already been generalized, taking into account the ion contribution [Issautier et al., 1999], in order to be routinely used on Ulysses [Issautier et al., 1998]. This extension of the method has been recently implemented on Wind, thereby improving the QTN determination of the core electron temperature (obtained to better than 10%), especially for high-speed solar wind flows ($V_{SW} \geq 500$ km s^{-1}).

In what follows we use the TNR electron density obtained by the neural network (which is in very good agreement with the one obtained by the fit) and the electron temperature obtained by the QTN spec-

troscopy method; we refer to these quantities as the TNR electron density and temperatures.

2.2. Wind 3-D Plasma Experiment

The Wind 3-D Plasma experiment [Lin et al., 1995] is designed to make measurements of the full three-dimensional distribution of electrons and ions from energies of the order of those of the thermal solar wind plasma to those of low-energy cosmic rays, with a high sensitivity, wide dynamic range, good energy and angular resolution and high time resolution. A pair of electron electrostatic analyzers (EESA-low (L) and EESA-high (H)) cover different parts of the electron population. In normal modes of operation the EESA-L instrument measures the electrons from a few eV to 1.1 keV and EESA-H measures from $\sim$100 eV to 30 keV (energy resolution $\sim$20 %), with 15 logarithmically spaced energy steps and full 4π angular coverage in one spacecraft rotation ($\sim$3 s). The data are combined on board into 88 angular bins, each with roughly $22° \times 22°$ resolution. These instruments provide full 3-D electron distributions and also onboard computed moments (density, velocity, pressure, temperature, and heat flux) with a very high time resolution ($\sim$3 s). Because of the allowed telemetry rate, only the onboard computed electron moments are transmitted routinely every 3 s. The full 3-D velocity distribution functions are transmitted only every $\sim$99 sec (for the time period considered in this paper).

We shall use in what follows the usual definitions of the lowest-order moments of an electron distribution $f(\mathbf{v})$:
- the number density N_e,

$$N_e = \int f(\mathbf{v}) \, d^3v, \qquad (1)$$

- the bulk flow velocity vector $\mathbf{V_e}$,

$$\mathbf{V_e} = \frac{1}{N_e} \int \mathbf{v} \, f(\mathbf{v}) \, d^3v, \qquad (2)$$

- the pressure tensor $\mathbf{P_e}$,

$$\mathbf{P_e} = m_e \int (\mathbf{v} - \mathbf{V_e})(\mathbf{v} - \mathbf{V_e}) \, f(\mathbf{v}) \, d^3v, \qquad (3)$$

- the heat flux vector $\mathbf{Q_e}$,

$$\mathbf{Q_e} = \frac{m_e}{2} \int (\mathbf{v} - \mathbf{V_e}) \cdot (\mathbf{v} - \mathbf{V_e})(\mathbf{v} - \mathbf{V_e}) \, f(\mathbf{v}) \, d^3v. \quad (4)$$

The thermal pressure p_e can be used to define the kinetic temperature of the electron plasma component ($p_e = N_e \, k_B \, T_e$),

$$T_e = \frac{m_e}{3 \, k_B \, N_e} \int (\mathbf{v} - \mathbf{V_e}) \cdot (\mathbf{v} - \mathbf{V_e}) \, f(\mathbf{v}) \, d^3v. \quad (5)$$

From the matrix of count rate samples, $C_{ijk} = C(E_i, \phi_j, \theta_k)$, collected by EESA-L every spacecraft

spin, the moments can then be computed, either on board or on ground, according to the definitions given above, by noting that for an electrostatic analyzer,

$$f_{ijk} \propto C_{ijk}/v_{ijk}^4, \qquad (6)$$

with a proportionality factor given by the detector response function; the limit of integration is between the two cutoff velocities $v_{\min}$ and $v_{\max}$ associated with the low- and high-cutoff energies, $E_{\min}$ and $E_{\max}$, respectively (where $E_{\min} = m_e v_{\min}^2/2$ and $E_{\max} = m_e v_{\max}^2/2$). As $v_{\max}$ is generally many times greater than the electron thermal velocity and flow velocity, it is practically infinity. The integrations are replaced by summations, and usually the assumption is made that $f(\mathbf{v})$ is constant over the integration volume elements, $d^3v = v^2 dv d\Omega = v^3 \, (dv/v) \, d\Omega$, with $dv/v = 0.5 \, dE/E \approx 0.16$.

For the period of interest in this paper (from June 1 to 26, 1995; see section 3), the EESA-L instrument has transmitted a total of 15×88 count rate samples (available every $\sim$99 s), which we have used to compute "on-ground" moments (namely, the density $N_{e\,\mathrm{df}}$, the bulk velocity $V_{e\,\mathrm{df}}$, the pressure $\mathbf{P}_{e\,\mathrm{df}}$, the temperature $T_{e\,\mathrm{df}}$, and the heat flux $\mathbf{Q}_{e\,\mathrm{df}}$, where the index df means computed with the distribution function); the low-energy threshold was $E_{\min} = E_0 - \delta E_0/2$, $E_0 = 11.47$ eV being the central value of the first energy step, whose width δE_0 is $\sim$3.65 eV, so that $E_{\min} \sim 9.65$ eV.

On the other hand, the thermal noise receiver (see section 2.1) provides measurements of the electron density every 4.5 s; thus it was interesting to compare this TNR density with the 3DP high-resolution electron density, calculated on board every 3 s. We have therefore checked for a relatively long period of time (roughly 1 month) whether the available 3DP high-resolution electron moments (namely, the density $N_{e\,3\mathrm{s}}$, the total velocity $V_{e\,3\mathrm{s}}$, the pressure $\mathbf{P}_{e\,3\mathrm{s}}$, the temperature $T_{e\,3\mathrm{s}}$, and the heat flux $\mathbf{Q}_{e\,3\mathrm{s}}$, where the index 3s indicates electron moments calculated on board) are compatible with moments obtained directly by integrating the 3DP electron distribution functions. We have found that this is indeed the case for the lowest-order moments, the densities, $N_{e\,3\mathrm{s}}$ and $N_{e\,\mathrm{df}}$, the velocities, $V_{e\,3\mathrm{s}}$ and $V_{e\,\mathrm{df}}$, and the temperatures $T_{e\,3\mathrm{s}}$ and $T_{e\,\mathrm{df}}$, but not for the individual components of the pressure tensor $\mathbf{P}_{e\,3\mathrm{s}}$ and $\mathbf{P}_{e\,\mathrm{df}}$ as well as for the heat fluxes $\mathbf{Q}_{e\,3\mathrm{s}}$ and $\mathbf{Q}_{e\,\mathrm{df}}$. The important conclusion of this analysis is that the 3DP experiment provides reliable, high-resolution (3 s) measurements of the density, velocity, and temperature of the solar wind electrons.

3. A 3DP/TNR Electron Density Comparison

Let us now compare the TNR electron density measurements given by the neural network $N_{e\,\mathrm{TNR}}$ and the 3DP uncorrected electron densities computed on board $N_{e\,3\mathrm{s}}$. The comparison has been made for a limited
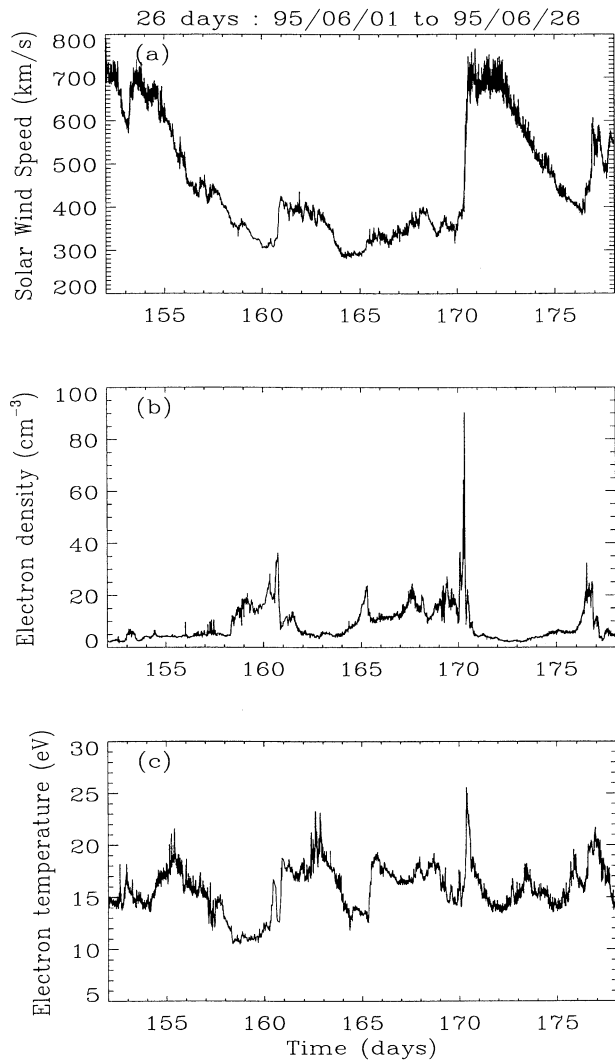
Figure 1. Synopsis of the solar wind parameters from June 1 to 26, 1995. The numbers indicate the beginning of the corresponding day of the year (June 1 = 152). (a) Solar wind speed in km s^{-1} from the three-dimensional plasma (3DP) experiment (proton data). (b) Electron density in cm^{-3} from the thermal noise receiver (TNR). (c) Electron temperature in eV (3DP electron data).

period of 26 days, June 1 to 26, 1995 (7 months after launch of Wind), when Wind was at > 200 R_E from Earth (in the free solar wind). This period is well suited to such a comparison, since it exhibits a large range of variations of the physical properties of the solar wind. As illustrated in Figure 1a, which displays the solar wind speed (the 3DP proton velocity) as a function of time, Wind crossed two high-speed flows and spent a long interval of time in a relatively low-speed wind. The numbers indicate the corresponding day of the year (day 152 = June 1, 1995). As shown in Figures 1b and 1c, the solar wind electron density (from TNR) ranges from ~2.5 to 90 cm^{-3}, while the electron temperature (from 3DP) ranges between ~10 and 25 eV. Note that to draw these plots, we used ~1-min resolution data and that N_e TNR was interpolated in order to get TNR and 3DP measurements at the same times.

Figure 2 displays a scatterplot of $N_{e\,3s}$ as a function of $N_{e\,TNR}$ for the period considered, containing 748,800 data points (26 days × 28,800 points day^{-1}). The two densities are significantly different: 3DP slightly overestimates the density for small densities and underestimates it for larger densities (when $N_e \geq 5$ cm^{-3}), even more as the density increases. This can be simply explained if we recall that we have used raw densities $N_{e\,3s}$, uncorrected for spacecraft charging, photoelectrons, and the low-energy cutoff of the electron spectrometer.

To illustrate what happens, Figure 3 shows schematically an electron distribution function $f(E)$ in the vicinity of the spacecraft surface, which is the sum of the photoelectron and the ambient solar wind electron distributions. Both populations are assumed here to be Maxwellian, the photoelectrons having typical density N_{ph} and temperature T_{ph} of ~500 cm^{-3} and 2 eV, respectively [see *Grard*, 1973], while three different cases are considered for the solar wind electron distribution perturbed by the S/C potential: Figure 3a corresponds to a high-density solar wind ($N_e = 40$ cm^{-3} and $T_e = 10$ eV), Figure 3b to an intermediate-density solar wind ($N_e = 15$ cm^{-3} and $T_e = 15$ eV), and Figure 3c to a low-density solar wind ($N_e = 2$ cm^{-3} and $T_e = 22$ eV). Before proceeding further, let us recall that in the solar wind, the photoelectrons emitted by the S/C body are usually dominant compared to the ambient electrons it collects. Thus the spacecraft charges positively, reaching a potential ϕ with respect to the plasma. As a consequence, the photoelectrons with energies smaller than $e\phi$ return to the surface and may be collected by the detector; only those emitted with an energy larger than $e\phi$ can escape into the plasma. Simultaneously, the incident solar wind electrons gain an energy $e\phi$, and their density is higher by a factor $\exp(e\phi/k_B T_e)$ at the surface of the spacecraft than far from it. Thus, neglecting
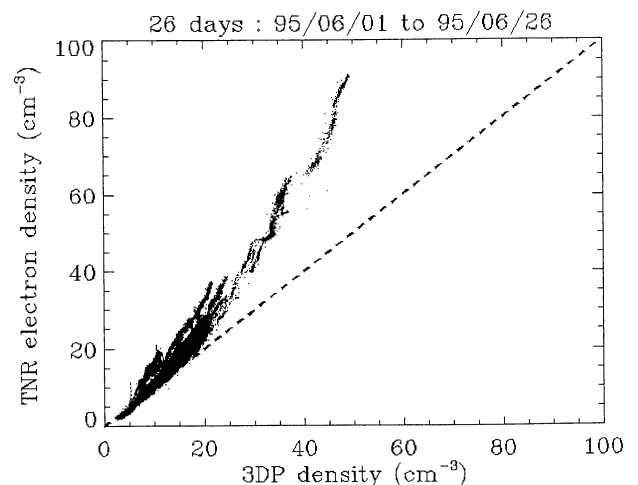
Figure 2. Scatterplot of the TNR electron density $N_{e\,TNR}$ (cm^{-3}) versus the raw 3DP electron density $N_{e\,3s}$, over 26 days. The diagonal line is shown by the dashed line.
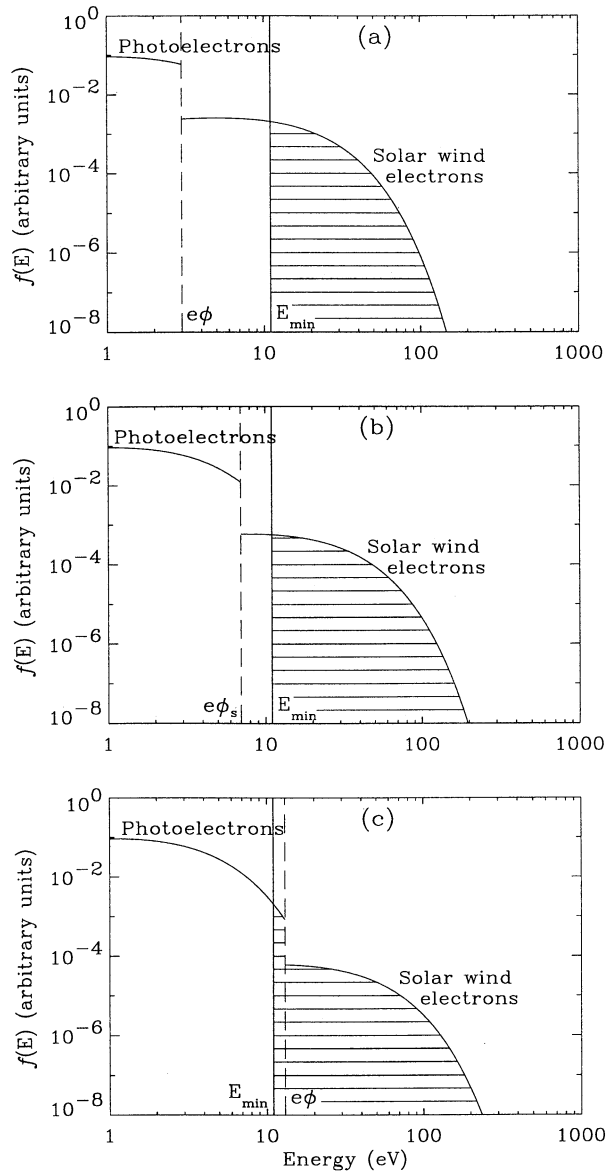
Figure 3. Sketch of an electron distribution function measured at a spacecraft, positively charged to an electrical potential ϕ, representing two different population of electrons (taken as Maxwellians here): photoelectrons (with a density $N_{ph} = 500$ cm^{-3} and a temperature $T_{ph} = 2$ eV) emitted at the spacecraft with energies below $e\phi$ and ambient electrons with energies increased by $e\phi$. $E_{\min}$ is the low-cutoff energy of the detector. Three different cases considered: (a) $e\phi < E_{\min}$, so that the density measured by the detector (hatched surface) is underestimated; (b) $e\phi = e\phi_s < E_{\min}$, so that the density measured by the detector (hatched surface) is just equal to the real density; and (c) $e\phi > E_{\min}$, so that the density measured by the detector (hatched surface) is overestimated.

any anisotropy, no ambient electrons with energies below $e\phi$ will be collected by the detector. As a result, the temperature of the solar wind electrons will also be affected by the S/C potential, since the mean random energy of the electrons is slightly higher in the vicinity of the spacecraft than far from it. In the first case (Figure

3a), $e\phi$ is much smaller than the 3DP/EESA low-energy cutoff $E_{\min}$ ($\sim$9.65 eV), so that the measured density (hatched area) is smaller than the true solar wind density. Because the solar wind electron density near the surface of the spacecraft is higher than far from it, there is a threshold of potential ϕ_s below $E_{\min}$, for which the measured density is equivalent to the true one (Figure 3b). For any S/C potential $\phi > \phi_s$, the measured density will be higher than the true solar wind density, particularly for $e\phi > E_{\min}$ (Figure 3c), because of the contribution of part of the low-energy photoelectrons.

As a result, the discrepancy between the TNR and 3DP measurements at small densities ($N_e \leq 10$ cm^{-3}) seems to be due to both the spacecraft charging and low-energy cutoff, $E_{\min}$, of the 3DP electron analyzers, while at high densities it appears to be mainly related to the existence of a low-energy cutoff, spacecraft charging being negligible.

It is then interesting to try to quantify the difference between $N_{e\,\text{TNR}}$ and $N_{e\,3s}$ and to correct accordingly the raw 3DP density. As explained in the introduction, the problem of correcting particle detector measurements without the help of data from other experiments has been extensively studied. However, these "internal" corrections require a significant amount of work, while the comparison with thermal noise measurements is very easy to implement, as we see in what follows. In principle, such corrections could be applied to any situation where particle detectors are operating simultaneously with a radio receiver capable of measuring thermal noise with sufficient sensitivity.

4. Scalar Correction Model for the Electron Moments

In what follows we show that a very effective and inexpensive way of performing these corrections can be achieved with the help of QTN spectroscopy. For that we begin by developing a very simple model in order to set up a "scalar correction" of the electron moments as measured by an electron spectrometer, taking into account the effects of both spacecraft charging and low-energy cutoff of the spectrometer (neglecting, at this stage, any other instrumental effects inherent to particle detectors). We proceed here along a path similar to that used by *Song et al.* [1997], our basic aim here being to extract, from simple analytic formulas, the basic trends of these scalar corrections as the plasma parameters vary. We therefore assume the following:

1. The electron spectrometer is a point source of electric potential $\varphi(r)$ in the ambient plasma ($\varphi(0) = \phi$, $\varphi = 0$ at infinity), implying spherical symmetry around the point source, all quantities depending only on the radial coordinate r.

2. The particle trajectories are purely radial, so that the conservation of total energy reduces to

$$v^2 = v'^2 - v_\phi^2, \qquad (7)$$

v' being the velocity, at the detector, of an incident particle of velocity v at infinity, and

$$v_\phi^2 = \frac{2e\phi}{m_e}. \tag{8}$$

3. The detector has a low-energy cutoff at energy $E_{\min}$, corresponding to a minimum speed $v_{\min} = (2E_{\min}/m_e)^{1/2}$.

4. This minimum speed satisfies $v_{\min} > v_\phi$, a condition always verified for $E_{\min} \simeq 10$ eV, as we show later (see section 5).

5. The solar wind electron distribution far from the spacecraft is a simple Maxwellian distribution (neglecting the high-energy electrons) at rest in the spacecraft frame, since the solar wind velocity V_{e0} is always small compared to the electron thermal velocity v_{th} at 1 AU $(1/2 \, m_e V_{e0}^2 \ll k_B T_{e0})$,

$$f(v) = \frac{N_{e0}}{\pi^{3/2} v_{th}^3} \exp\left(-\frac{v^2}{v_{th}^2}\right), \tag{9}$$

with density N_{e0} and temperature T_{e0},

$$v_{th} = \left(\frac{2 \, k_B T_{e0}}{m_e}\right)^{1/2}. \tag{10}$$

As mentioned in section 2.1, the real electron distribution function is actually not a simple Maxwellian. The commonly used model to represent the observed distributions is a sum of two Maxwellians, a core and a halo, with a halo component contributing to only ~5% of the total electron density and to ~20% of the total temperature [Feldman et al., 1975; Pilipp et al., 1987]. Those percentages are roughly comparable to the uncertainties of the determination of the electron density and temperature from the thermal noise analysis. Therefore the use of a simple Maxwellian distribution as a zero-order approximation of the real distribution is relevant to our model.

Note that when assumption (4) is valid, no photoelectron can be measured by the detector, so that this population may be safely ignored in this model. The "raw" electron density N_e and temperature T_e are then given by

$$N_e = 4\pi \int_{v^*}^{\infty} v'^2 \, f'(v') \, dv', \tag{11}$$

$$T_e = \frac{4\pi \, m_e}{3 \, k_B \, N_e} \int_{v^*}^{\infty} v'^4 \, f'(v') \, dv', \tag{12}$$

where

$$v^* = \max(v_{\min}, v_\phi). \tag{13}$$

The distribution function at the particle detector, $f'(v')$, can be expressed as a function of the distribution $f(v)$ at infinity:

$$f'(v') = f(v). \tag{14}$$

Using the conservation of energy (equation (7)), this leads to

$$f'(v') = \frac{N_{e0}}{\pi^{3/2} v_{th}^3} \, e^{e\phi/k_B T_{e0}} \, e^{-v'^2/v_{th}^2}, \tag{15}$$

with $v' \geq v_\phi$. Since we are assuming $e\phi < E_{\min}$ (so that $v^* = v_{\min}$), both expressions (equations (11) and (12)) can be rewritten after simple manipulations as

$$N_e = N_{e0} \, e^{u_\phi^2} \left[1 - \text{erf}(u_{\min}) + \frac{2}{\sqrt{\pi}} u_{\min} e^{-u_{\min}^2}\right], \tag{16}$$

$$T_e = T_{e0} \left[1 + \frac{4}{3\sqrt{\pi}} \times \left(\frac{u_{\min}^3 \, e^{-u_{\min}^2}}{1 - \text{erf}(u_{\min}) + \frac{2}{\sqrt{\pi}} \, u_{\min} e^{-u_{\min}^2}}\right)\right], \tag{17}$$
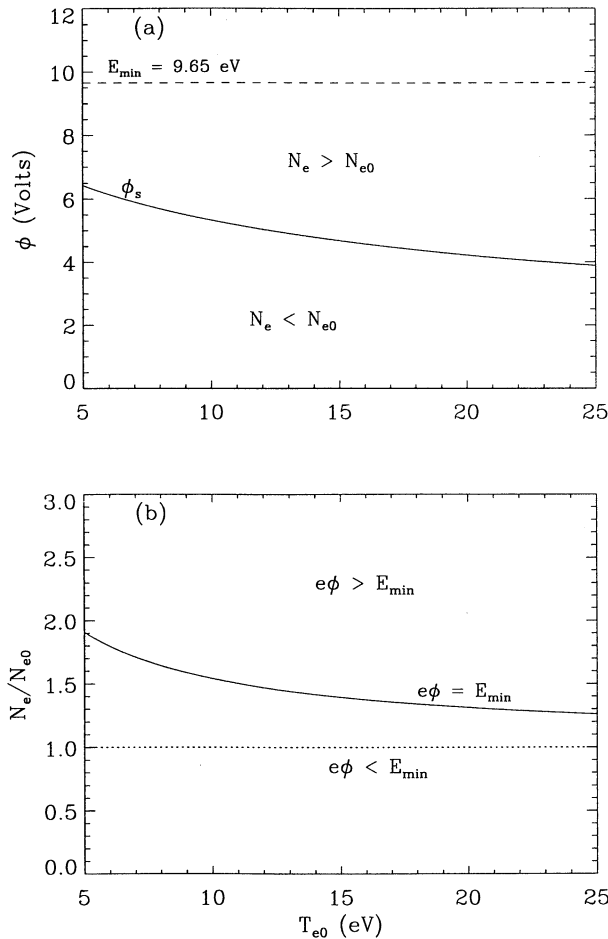
where

$$u_\phi = \frac{v_\phi}{v_{th}} = \left(\frac{e\phi}{k_B T_{e0}}\right)^{1/2}, \tag{18}$$

$$u_{\min} = \frac{v_{\min}}{v_{th}} = \left(\frac{E_{\min}}{k_B T_{e0}}\right)^{1/2}. \tag{19}$$

We see that N_e/N_{e0} depends on both the spacecraft potential and the low-energy cutoff of the electron spectrometer, whereas T_e/T_{e0} does not depend explicitly either on the density nor on the S/C potential, but it is affected by the missing electrons between 0 and $E_{\min}$, even in the case where all the solar wind electron distribution is sampled (for $e\phi = E_{\min}$).

It may be seen in (16) that there is a value $\phi = \phi_s$ (smaller than $E_{\min}$) of the S/C potential depending on $u_{\min}$, i.e. on $E_{\min}$ and T_{e0}, for which $N_e = N_{e0}$, even if only part of the electron population is sampled; this is the case represented schematically in Figure 3b. The same equation shows also that for given values of $E_{\min}$ and T_{e0}, N_e will be smaller (greater) than N_{e0} if ϕ is smaller (Figure 3a) (greater, Figure 3c) than ϕ_s. The variation of ϕ_s with T_{e0} is shown in Figure 4a, for $E_{\min} = 9.65$ eV. In addition, Figure 4b shows how much the measured density is overestimated in the case where the potential reaches the low-energy cutoff $(e\phi = E_{\min})$: the ratio N_e/N_{e0} is displayed as a function of T_{e0}, also for $E_{\min} = 9.65$ eV. This condition could be met for very low solar wind densities, so that N_e/N_{e0} could reach ~1.5. The domain above the curve (Figure 4b) corresponds to $e\phi > E_{\min}$, and the one below it corresponds to $e\phi < E_{\min}$.

The S/C potential depends on both the electron density N_{e0} and temperature T_{e0}; in Appendix A, we derive an expression for ϕ (equation (A7))b from a balance between the photoelectron current and the solar wind electron current, depending on the electron density N_{e0}, the electron temperature T_{e0}, and three other parameters. These are the photoelectron temperature T_{ph}, a parameter χ depending on the spacecraft material, and the solar distance d_{AU} (in astronomical units), all of which here are given fixed values, $T_{ph} = 2$ eV, $\chi = 2$, and $d_{AU} = 1$ AU. Note that, on the basis of this

function of T_e (equation (17)) for $E_{min} = 9.65$ eV, the diamonds being the corresponding best linear fit,
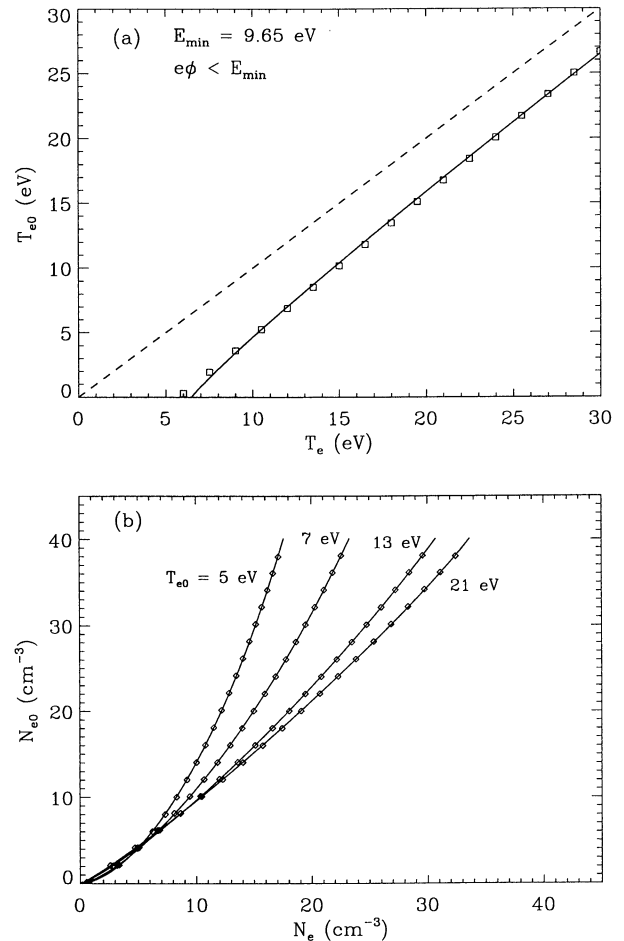
$$T_{e0} = -5.97 + 1.09\, T_e, \qquad (21)$$

and the dashed line representing the diagonal line. Since the ratio T_e/T_{e0} (equation (17)) is found to be simply proportional to u_{min}^2 $(T_e/T_{e0} \propto u_{min}^2)$, the constant coefficient in the relation above is only due to E_{min}. For $E_{min} = 0$ (thus $\phi = 0$ because of the condition $e\phi < E_{min}$) we have verified that $T_{e0} = T_e$.

The approximate solution for N_{e0} has the form of a polynomial in N_e,

$$N_{e0} = \mu(T_{e0}) + \nu(T_{e0})\, N_e + \rho(T_{e0})\, N_e^2, \qquad (22)$$

as suggested by the nonlinear shape of the observed scatterplot of $N_{e\,3s}$ versus $N_{e\,TNR}$ (Figure 2), where the coefficients μ, ν, and ρ depend on T_{e0}. These coeffi-

Figure 4. (a) The critical potential ϕ_s for which $N_e = N_{e0}$ as a function of the electron temperature T_{e0}. (b) Ratio N_e/N_{e0}, in the case where $e\phi = E_{min}$, as a function of the electron temperature T_{e0}.

expression, the condition of the validity of the model, $0 \le e\phi \le E_{min}$, is met for $0 \le N_{e0} \le 40$ cm^{-3} (above 40 cm^{-3}, ϕ becomes negative) and for $7 \le T_{e0} \le 23$ eV.

Inserting this expression of the S/C potential into (16), N_e appears to be a function of N_{e0} and T_{e0} while T_e is only function of T_{e0}, for a given E_{min} (equation (16)):

$$N_e = F(N_{e0}, T_{e0}) \qquad (20a)$$

$$T_e = G(T_{e0}) \qquad (20b)$$

Equations (16), (17) and (A7) then form a complicated system of nonlinear equations for N_{e0} and T_{e0} (see (20b) and (20b)) in terms of the raw moments N_e and T_e, which cannot be simply inverted analytically in order to get N_{e0} and T_{e0} as functions of the measured moments N_e and T_e. Therefore we have tried to obtain approximate, but simple forms of the solution, valid in the range $0 \le N_{e0} \le 40$ cm^{-3} and $7 \le T_{e0} \le 23$ eV as described above. First, (17) can be simply approximated by a linear relation between T_{e0} and T_e, in the range considered here. Figure 5a displays T_{e0} as a

Figure 5. (a) The real temperature T_{e0} as a function of the measured one (see equqtion (17)), for $E_{min} = 9.65$ eV (solid line). The diamonds are the corresponding best linear fit (equation (21)), and the dashed line is the diagonal line. (b) N_{e0} as a function of N_e for different values of $T_{e0} = 5$, 7, 13, and 21 eV. Solid lines are the exact solutions of equation (16), whereas the diamonds are the approximate solutions (equation (22)).
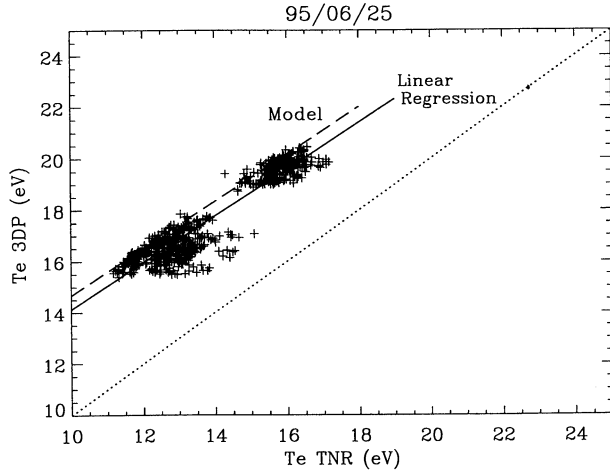
Figure 6. Scatterplot of the 3DP electron temperature, $T_{e\,df}$, versus the TNR electron temperature $T_{e\,TNR}$, on June 25, 1995 (data points represented by crosses). The solid line is a linear fit, and the dashed line is the prediction of the model (equation (21)).

cients are themselves polynomials in $1/T_{e0}$ to take into account the observed fact (not shown here) that, globally, the ratio $N_{e\,3s}/N_{e\,TNR}$ increases with increasing temperature, so that temperature does seem to play a decreasing role for large values of N_e:

$$\mu(T_{e0}) = 0.48 - 20.61/T_{e0} + 86.27/T_{e0}^2 \quad (23a)$$

$$\nu(T_{e0}) = 0.84 + 2.30/T_{e0} - 20.87/T_{e0}^2 \quad (23b)$$

$$\rho(T_{e0}) = 0.01 - 0.16/T_{e0} + 2.73/T_{e0}^2 \quad (23c)$$

The values of the various coefficients have been obtained by a best fit between the direct numerical solutions of (16) (combined with (A7)) and the approximate one (equation (22)), in the case when $E_{min} = 9.65$ eV. Examples are displayed in Figure 5b for $T_{e0} = 5$, 7, 13, and 21 eV; the solid lines are the exact numerical solutions, and the diamonds are the corresponding approximate solutions. Note the similarities between these "theoretical" curves and the scatterplot of Figure 2, i.e., their parabolic shape, the various branches corresponding to different temperatures, as well as the overestimation and underestimation of the density, respectively, for small and large densities.

Equations (21) and (22) provide simple correction formulas relating the raw moments to the actual values in the plasma, far from the spacecraft. Let us stress once again that they are valid for $e\phi < E_{min}$ and that the coefficients depend appreciably on E_{min}; besides, they have been obtained within the framework of a very simple model, so that the best one can hope is that they are qualitatively correct, the precise value of the numerical coefficients appearing in these correction formulas varying with the geometry of the spacecraft, the detector, etc, or with any other instrumental effects.

This can be checked by using the 3DP high-resolution moments calculated on board ($N_{e\,3s}$ and $T_{e\,3s}$) and the

TNR electron density and temperature ($N_{e\,TNR}$ and $T_{e\,TNR}$) identified as the true electron density and temperature (N_{e0} and T_{e0}). This has been done for the period of 26 days considered previously (June 1 to 26, 1995), during which the low-energy threshold of the detector is $E_{min} = 9.65$ eV. We considered only the data points such as $N_{e\,TNR} \leq 40$ cm^{-3} in order to always remain within the limit of validity of the correcting formulas (equations (21), (22), and (23b)-(23c)).

In the present stage of data reduction, a large, comprehensive set of TNR electron temperatures is not yet available, so that we have limited our comparison to June 25, 1995, as far as temperatures are concerned. Figure 6 displays the 3DP electron temperature as a
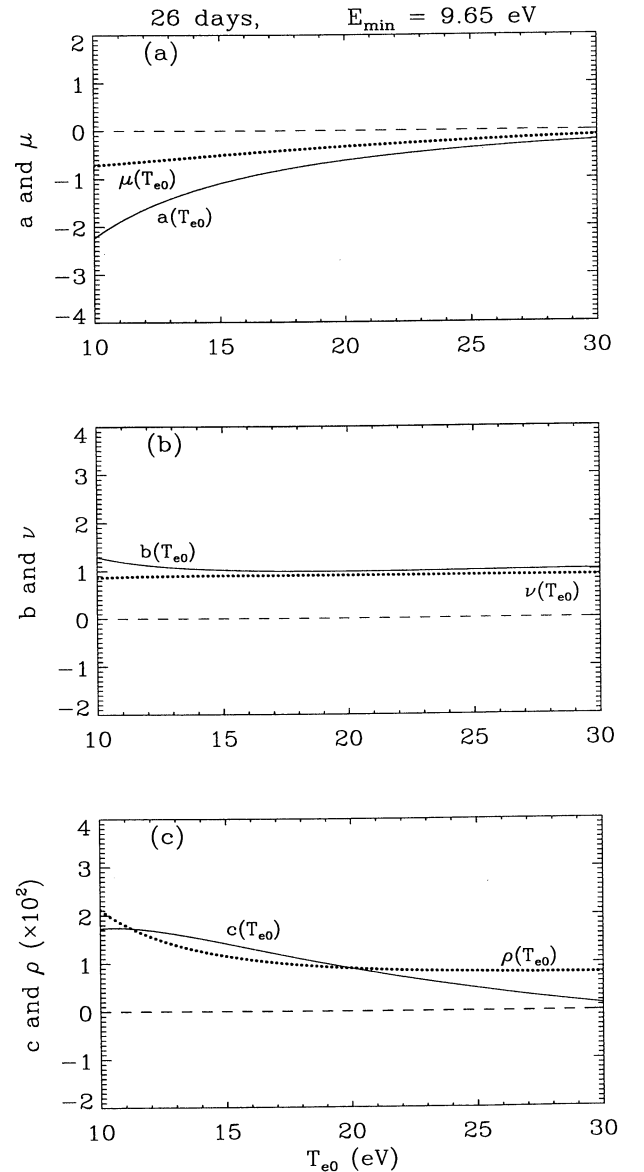
Figure 7. Variations of the "theoretical" (equations (23a)-(23c)) and the "experimental" (equation (26a)-(26c)) sets of coefficients (a) μ and a, (b) ν and b, and (c) ρ and c, with the electron temperature, shown by dotted and solid lines, respectively.

Table 1. Coefficients of Equation (27) for Different Low-Energy Thresholds E_{min}

	June 1-26, 1995, $E_{min} = 9.65$ eV	July 7-21, 1995, $E_{min} = 5.46$ eV
a_0	5.368 ± 0.115	7.063 ± 0.631
a_1	-103.680 ± 2.074	-150.283 ± 5.874
a_2	-24.987 ± 16.432	247.408 ± 32.869
b_0	1.411 ± 0.011	0.259 ± 0.030
b_1	-36.397 ± 0.358	9.608 ± 0.690
b_2	480.575 ± 2.870	-20.372 ± 3.958
c_0	-0.0228 ± 0.0004	0.028 ± 0.001
c_1	1.594 ± 0.015	-0.442 ± 0.020
c_2	-14.754 ± 0.122	2.180 ± 0.116

function of the TNR one (crosses correspond to data points). The solid line is a simple linear regression made over all the data points,

$$T_{e\,\text{TNR}} = -5.52 + 1.10\,T_{e\,3s},\qquad (24)$$

whereas the dashed line shows the prediction of the model (equation (21)), which does a very good job, except for a small systematic difference of ~ 0.5 eV, probably due to the electron bulk velocity, which is not zero as assumed in the model.

For density comparisons we take advantage of this good agreement and determine first a "corrected" 3DP temperature $T_{ec\,3s}$ (the index c meaning *corrected*) using (24). We then fit a polynomial of $N_{e\,3s}$ (of the form given by (22)) to the density $N_{e\,\text{TNR}}$,

$$N_{e\,\text{TNR}} = a(T_{ec\,3s}) + b(T_{ec\,3s})\,N_{e\,3s} + c(T_{ec\,3s})\,N_{e\,3s}^2, \quad (25)$$

where a, b and c are polynomials of $1/T_{ec\,3s}$ of the form given by (23b)-(23c):

$$a(T_{ec\,3s}) = a_0 + a_1/T_{ec\,3s} + a_2/T_{ec\,3s}^2, \quad (26a)$$
$$b(T_{ec\,3s}) = b_0 + b_1/T_{ec\,3s} + b_2/T_{ec\,3s}^2, \quad (26b)$$
$$c(T_{ec\,3s}) = c_0 + c_1/T_{ec\,3s} + c_2/T_{ec\,3s}^2. \quad (26c)$$

A multiple linear regression fit, with 745,750 data points, is done over all the period to determine the nine coefficients with good precision, given the large number of data points. As a result, Figure 7 displays the variation of the "theoretical" coefficients (μ, ν and ρ of (23b)-(23c); dotted lines) with the electron temperature $T_{e0} = T_{ec\,3s}$, compared to variations of the "experimental" set of coefficients (a, b and c of (26b)-(26c); solid lines). It is seen that both sets of coefficients are comparable and behave similarly, giving some confidence that the correcting formulas (21), (22), and (23b)-(23c) contain the essential effects to affect the particle detector measurements.

We now extend the comparison outside the limits of our simple model. First, since there is a linear relation between the raw electron temperature and the actual one, it is more practical to use directly the former one in (25),

$$N_{e\,\text{TNR}} = a(T_{e\,3s}) + b(T_{e\,3s})\,N_{e\,3s} + c(T_{e\,3s})\,N_{e\,3s}^2. \quad (27)$$

Then, the multiple linear regression fit is redone using directly $T_{e\,3s}$, now with all of the data points (i.e., 748,800 data points; see section 3.2), even for densities above 40 cm^{-3}. The coefficients obtained by the fit are given in Table 1; note that they are somewhat different from those obtained above.

Adopting these coefficients, we then corrected the 3DP density $N_{e\,3s}$ (displayed in Figure 2) using (27). With the same format, we display in Figure 8a a scatterplot of the corrected 3DP density $N_{ec\,3s}$ as a function of the TNR density $N_{e\,\text{TNR}}$. Comparing Figures 2 and 8a, it is now evident that all the data points are distributed along the diagonal line, with small scatter. Only 0.4% of our sample corresponds to a density > 40 cm^{-3}, so that the fluctuations around the diagonal for densities > 40 cm^{-3} may not be significant. The agreement between the two densities is very good; their difference,
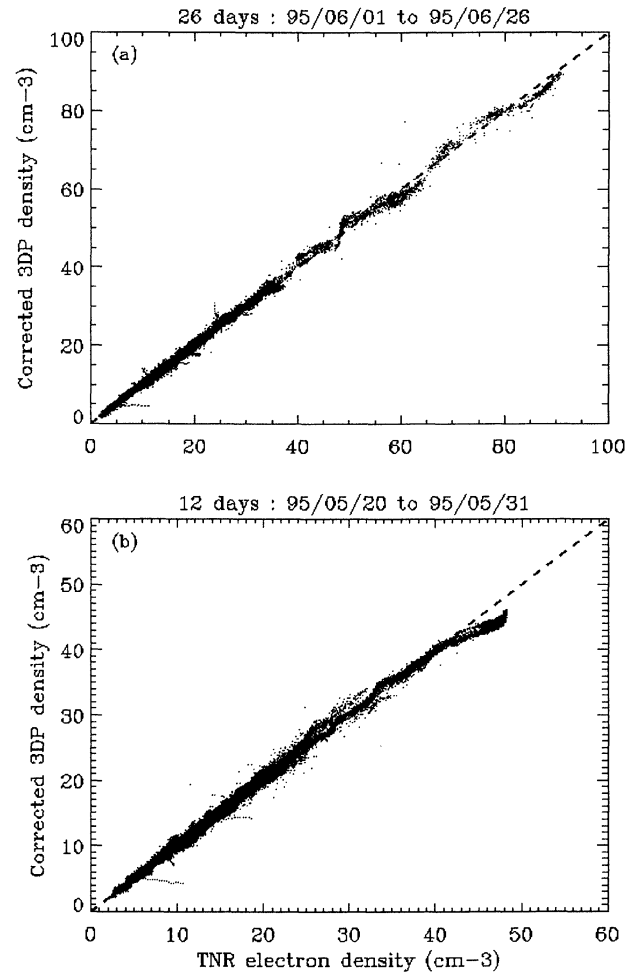
Figure 8. Scatterplot of the 3DP high-resolution electron density $N_{ec\,3s}$, corrected using equation (27), versus the TNR electron density for (a) June 1 to 26, 1995, and (b) May 20 to 31, 1995. In both cases, all the data points are distributed along the diagonal.
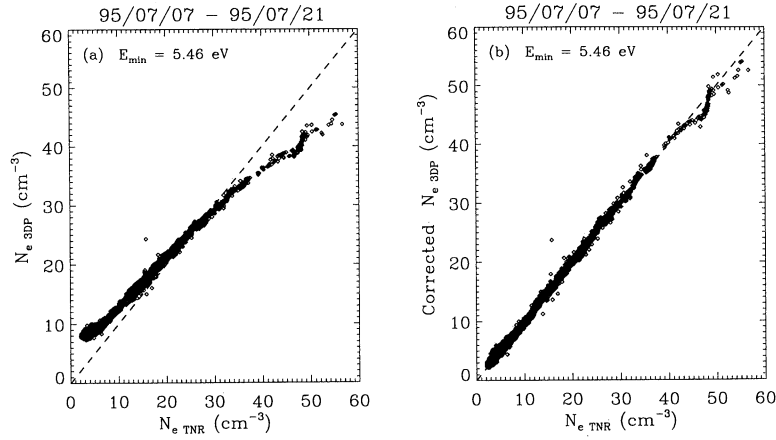
Figure 9. Scatterplots of the (a) raw and (b) corrected 3DP electron density, using the correction law with the coefficients given in Table 1, versus the TNR electron density for $E_{\min} = 5.46$ eV.

$$\delta N = \frac{N_{e\,\mathrm{TNR}} - N_{ec\,3s}}{N_{e\,\mathrm{TNR}}}, \qquad (28)$$

has an almost Gaussian distribution (for the 748,800 data points) with a standard deviation ~ 0.05 (or 5%), of the same order of the accuracy of the TNR density measurements, $\sim 4.4\%$ (see section 2.1). Here 90% of the data correspond to $|\delta N| < 7.5\%$. The 10% of the data for which $|\delta N| > 7.5\%$ correspond to values of the density close to the TNR band boundaries (A-C or C-E boundary), where the TNR density is determined with an accuracy of only 10%.

5. Semiempirical Correction Using QTN Spectroscopy

Before using routinely (24) and (27) to correct the raw moments $N_{e\,3s}$ and $T_{e\,3s}$, we must check that they predict correctly the electron density and temperature for time periods other than the period of 26 days used to calculate the coefficients of the fitting. As an example, we present in Figure 8b the comparison between $N_{e\,\mathrm{TNR}}$ and $N_{ec\,3s}$ (calculated using the coefficients of Table 1) for a period of 11 days, from May 20 to 31, 1995 (for which $E_{\min} \sim 9.65$ eV, as for the reference period); the agreement between the TNR density and the 3DP corrected density is very good, and the small deviations observed for densities around 45 cm^{-3} are due to a systematic overestimation of the TNR density by the neural network, on May 23, 1995, between 0730 UT and 1200 UT.

When the EESA-L mode of operation changes, i.e., when $E_{\min}$ changes significantly, it is expected that the values of the coefficients appearing in the correction formulas will change and that a new empirical "calibration" with the TNR data has to be performed. To illustrate this, we consider another period, July 7 to 21, 1995, during which $E_{\min} = 5.46$ eV. For this period also, the 3DP electron density and temperature are those calculated on board every ~ 3 s, $N_{e\,3s}$ and $T_{e\,3s}$.

Using the same technique, we obtain new coefficients, which are also reported in Table 1. Figure 9a displays the raw 3DP density versus the TNR one, while Figure 9b shows the density $N_{ec\,3s}$, corrected with (27) and the appropriate set of coefficients, versus $N_{e\,\mathrm{TNR}}$; it is seen that the correction formulas work very efficiently.

For a mode of operation with a low-energy threshold much smaller than $e\phi$ ($E_{\min} \ll e\phi$, as shown schematically in Figure 3c), as sometimes happens, the resulting electron density is much higher than the true one, and, conversely, the electron temperature is smaller than the true one. This is due to the contribution of the photoelectrons (which are cold relative to the solar wind electrons, $T_{ph} < T_{e0}$) with energies between $E_{\min}$ and $e\phi$. In this case, in order to be able to apply our correcting formulas, it is simplest to use in the moments' calculation a higher low-energy cutoff $E^*_{\min} > e\phi$ (i.e., and discard all energy steps below $E^*_{\min}$).

We can conclude that (1) the simple scalar correction model, described in the previous section, which takes into account the spacecraft charging and the low-energy cutoff effects, describes in a qualitative way the discrepancy between the raw particle moments and those obtained from QTN spectroscopy and that (2) it provides a simple way for correcting, with good accuracy, the electron density measured by the electrostatic analyzers. An important point is that one does not need to determine the spacecraft potential to perform the correction; this is replaced by the much simpler task of finding the nine coefficients appearing in the correction formulas (equation (27)), by fitting the raw densities and temperatures obtained by the particle detectors with the corresponding density from the QTN spectroscopy over a relatively small period of time chosen as a reference. As discussed above, the semiempirical relation obtained by this fit leads to a corrected electron density within 5%, as long as $E_{\min}$ remains unchanged. The corrected electron temperature can be obtained in the same way, by finding the two coefficients appearing in (24) over

26 days : 95/06/01 to 95/06/26
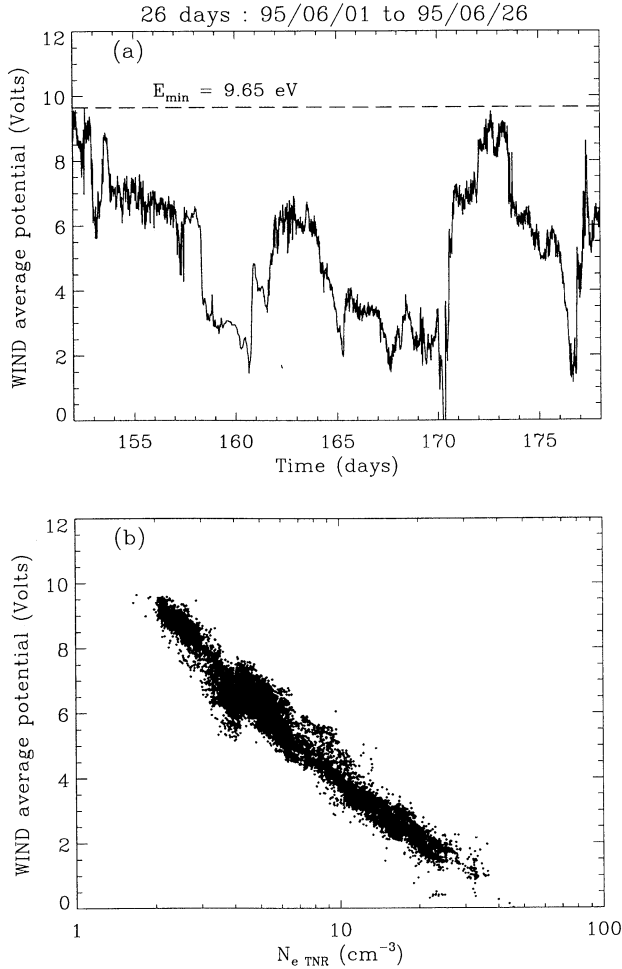
Figure 10. Wind electrical potential ϕ, as predicted by the model (deduced from equation (22)) using $N_{e\,\mathrm{TNR}}$, $N_{e\,3s}$ and $T_{e\,3s}$, (a) as a function of time (days) for the period of 26 days, from June 1 to 26, 1995, and (b) versus of the electron density $N_{e\,\mathrm{TNR}}$ represented in a logarithmic scale.

the same period; the corresponding relative uncertainty is of the order of 10%.

Note, however, that the model also predicts the spacecraft potential as function of density and temperature. Indeed, it can easily be obtained from (16) and (17), using $N_{e\,\mathrm{TNR}}$, $N_{e\,3s}$, and $T_{e\,3s}$. The result is shown in Figure 10a, which displays the Wind electric potential as a function of time, for the period of 26 days considered initially (from June 1 to 26, 1995), where $E_{\min} \sim 9.65$ eV, used here as a test period. The S/C potential exhibits a relatively large range of variations, between 0 and 10 V. One can notice that it reaches negative values during a short period of a few hours, during which the solar wind density was higher than 50 cm^{-3} (on June 19, 1995). This is in good agreement with the spacecraft potential calculated "theoretically", i.e., from a balance between photoelectron currents and ambient electron currents (equation (A7)). For reference, Figure 10b displays a scatterplot of the spacecraft potential versus the TNR density in a logarithmic scale:

the relation between ϕ and $log_{10}(N_{e\,\mathrm{TNR}})$ is close to linear, with some evidence of curvature. The S/C potential determined in this way can be used, for example, to correct the electron distribution functions themselves.

6. Electron Heat Flux

The simplified model described in section 4 assumes that the electron distribution function is an isotropic Maxwellian and therefore does not allow one to correct the raw electron bulk velocity, though, as discussed below, it is seriously affected by the spacecraft potential and the incomplete sampling of the core of the distribution (a nonzero $E_{\min}$), even more than the electron temperature. This can thus alter the determination of the electron heat flux.

6.1. Electron Velocity

We use in the following the electron moments (indexed by df) obtained by integrating the 3-D distribution functions, with a time resolution of 99 s. The 3DP electron velocity, $\mathbf{V}_{e\,df}$, exhibits large differences when compared to the proton velocity, $\mathbf{V}_p$, especially when $N_{e\,df}/N_{e\,\mathrm{TNR}}$ is smaller than unity. We use here, for $\mathbf{V}_p$, the 3DP high-resolution proton velocity (calculated on board), interpolated at the $\mathbf{V}_{e\,df}$ times. Let us then consider the difference between the electron and the proton velocities,

$$\delta\mathbf{V} = \mathbf{V}_e - \mathbf{V}_p. \tag{29}$$

By analyzing the azimuth of this drift and the azimuth of the ambient magnetic field **B**, we find that there is an electron-proton drift perpendicular, rather than parallel, to **B**. This corresponds to an angle between the directions of $\mathbf{V}_e$ and $\mathbf{V}_p$ of $\sim 20°$. We used for that the key parameters magnetic field data (with a resolution of 1.5 min), measured in the Magnetic Field Investigation (MFI) experiment [Lepping et al., 1995]. The magnetic field has also been interpolated at the $\mathbf{V}_{e\,df}$ time.

Can this systematic drift, in the direction perpendicular to **B**, be compensated by the alpha particles? We can check that by using the conditions of charge neutrality and zero current in the solar wind. For a plasma with several species the space charge σ and current density **j** are
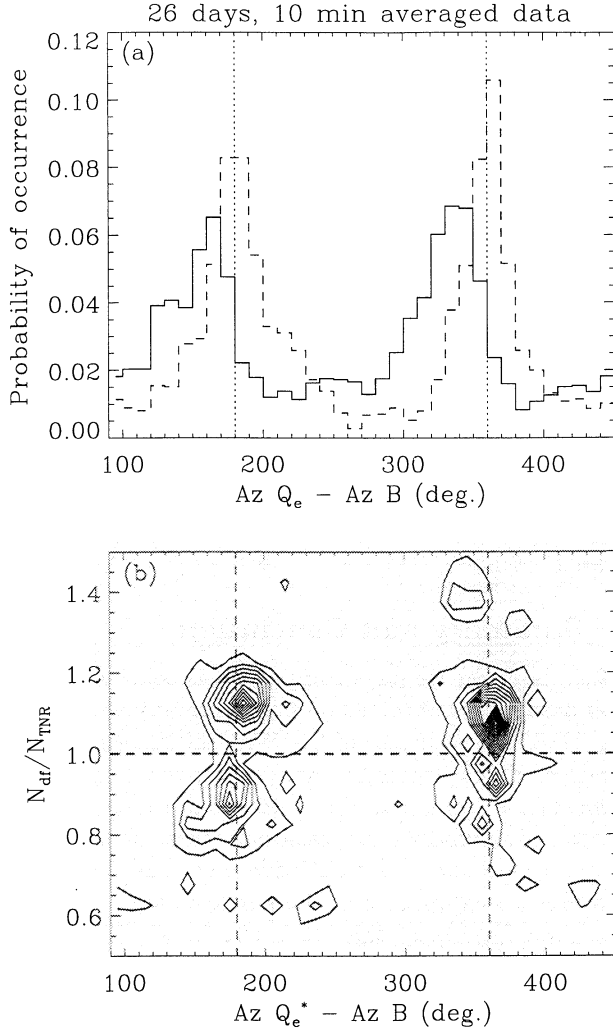
$$\sigma = \sum_i Z_i\, e\, N_i, \tag{30}$$

$$\mathbf{j} = \sum_i Z_i\, e\, N_i\, \mathbf{V}_i, \tag{31}$$

where $e = 1.6\,10^{-19}$ C is the elementary charge. In the solar wind the most abundant heavy ions are the alpha particles ($Z_\alpha = 2$). So the space charge and the current density are

$$\sigma = e\,(N_p + 2\,N_\alpha - N_e), \tag{32}$$

$$\mathbf{j} = e\,(N_p\,\mathbf{V}_p + 2\,N_\alpha\,\mathbf{V}_\alpha - N_e\,\mathbf{V}_e), \tag{33}$$

Figure 11. (a) Histogram of the difference $Az(\mathbf{Q}_e) - Az(\mathbf{B})$ in degrees, between the azimuth of the electron heat flux $\mathbf{Q}_e$ and the azimuth of the magnetic field $\mathbf{B}$ during the 26 days with 10 min averaged data. The solid line corresponds to the electron heat flux $\mathbf{Q}_e$ calculated with respect to the bulk electron velocity (as measured with $E_{\min} = 11$ eV), and the dashed line corresponds to the "corrected" electron heat flux $\mathbf{Q}_e^*$, calculated with respect to the bulk proton velocity. Here $180°$ corresponds to a heat flux antiparallel to $\mathbf{B}$, and $360°$ corresponds to a heat flux parallel to $\mathbf{B}$. (b) Contours of isoprobability of occurrence of a pair of values of $[Az(\mathbf{Q}_e^*) - Az(\mathbf{B}), N_{e\,\mathrm{df}}/N_{e\,\mathrm{TNR}}]$.

where the indices p, α and e represent the protons, the alpha particles, and the electrons, respectively. The conditions of charge neutrality and zero current, in the solar wind, are

$$\sigma \simeq 0 \,, \quad |\mathbf{j}| \simeq 0, \tag{34}$$

leading to

$$\mathbf{V}_e = \mathbf{V}_p + \Delta\mathbf{V}_\alpha, \tag{35}$$

where

$$\Delta\mathbf{V}_\alpha = \frac{2\,N_\alpha}{N_e}\,(\mathbf{V}_\alpha - \mathbf{V}_p). \tag{36}$$

The alpha particle contribution, $\Delta\mathbf{V}_\alpha$, is evaluated using (1) the TNR electron density $N_{e\,\mathrm{TNR}}$ as N_e, and (2) the SWE proton density from the key parameters $N_{p\,\mathrm{SWE}}$ (more accurate than the one given by the 3DP experiment because of a detector saturation problem with the 3DP proton electrostatic analyzer when the density is > 10 to 30 cm^{-3}), combined with the 3DP alpha to proton density ratio in order to get the alpha particle density N_α. This contribution is found to be much smaller than $\delta\mathbf{V}$ (equation (29)), i.e., about $\sim10^{-3}$ to $10^{-2}\,\mathbf{V}_p$, on average, so that the apparent perpendicular drift between electrons and protons cannot be due to the alpha particles. It is probably due to the uncertainty in the determination of the electron bulk velocity, due to the missing core electrons in the distribution function. One can thus consider the proton bulk velocity as a good approximation of the "true" electron bulk velocity. This is an important point for the determination of the electron heat flux.

6.2. Correcting the Electron Heat Flux

The 3-D electron heat flux (equation (4)) is calculated by a numerical integration from ~10 to 1200 eV for the 26 days considered. We only consider the heat flux vector $\mathbf{Q}_e$, i.e., the trace of the heat flux tensor in the GSE directions. This total electron heat flux $\mathbf{Q}_e$ is calculated with respect to the bulk velocity $\mathbf{V}_e$ of the whole electron population (equation (4)), without correction of the effects of the spacecraft potential and/or the low-energy cutoff and without separation of the core and halo electrons, as *Feldman et al.* [1975] did for the IMP 7 data. *Pilipp et al.* [1987] considered the 2-D electron distributions (on Helios) only for energies above 10 eV, in order to eliminate the photoelectrons, and corrected the electron heat flux (calculated with respect to the bulk electron velocity) by the ratio of the proton to electron density, while *Scime et al.* [1994b] calculated all the electron moments from the "vector-corrected" electron distributions (on Ulysses).

Our sample contains 3250 points, which are 10-min averages of the electron heat flux (125 points per day during 26 days). Figure 11a displays a histogram (solid line) of the difference between the azimuth of $\mathbf{Q}_e$ and the azimuth of $\mathbf{B}$, $Az(\mathbf{Q}_e) - Az(\mathbf{B})$, calculated between $90°$ and $270°$. If $\mathbf{Q}_e$ was statistically parallel or antiparallel to $\mathbf{B}$, the difference $Az(\mathbf{Q}_e) - Az(\mathbf{B})$ would be $360°$ or $180°$, respectively. However, this difference peaks close to $160°$ and $340°$: the azimuth of $\mathbf{Q}_e$ is systematically smaller (by $\sim20°$) than the azimuth of $\mathbf{B}$. Such a systematic deviation of the heat flux with respect to the direction of the magnetic field is contradictory to earlier studies [*Feldman et al.*, 1975; *Pilipp et al.*, 1987; *Scime et al.*, 1994b]. It may be related to the systematic error in the determination of the electron velocity, since we have calculated $\mathbf{Q}_e$ with respect to $\mathbf{V}_e$ (equation (4)). We argued above that the bulk proton velocity $\mathbf{V}_p$ is a better approximation of the bulk

26 days, 10 min averaged data
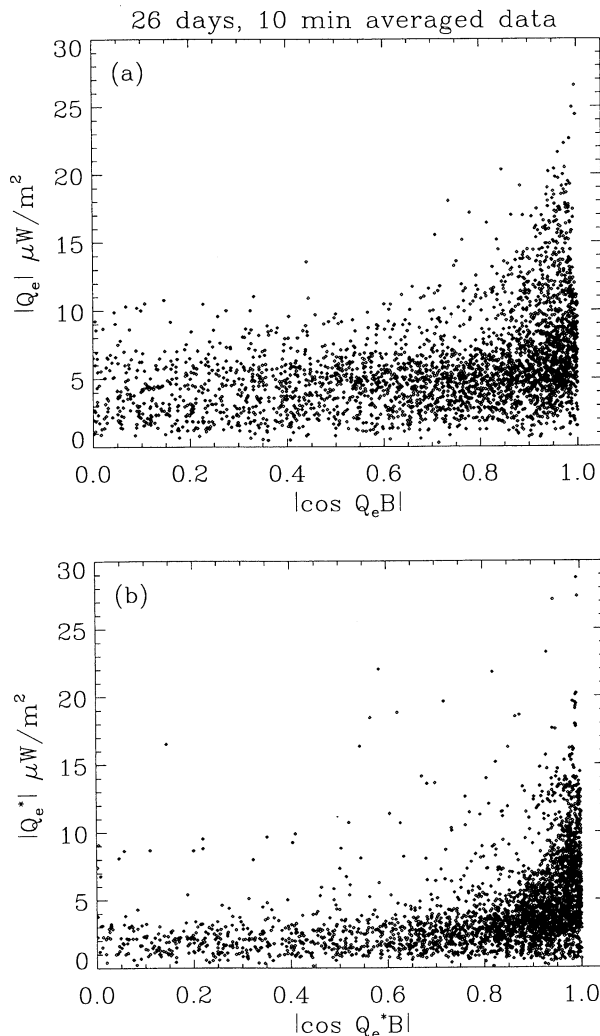
Figure 12. (a) Scatterplot of $\mathbf{Q}_e$ (calculated in the electron frame) as a function of the angle between $\mathbf{Q}_e$ and the magnetic field $\mathbf{B}$ during the 26 days with 10 min averaged data. (b) Scatterplot of $\mathbf{Q}_e^*$ (calculated in the proton frame) as a function of the angle between $\mathbf{Q}_e^*$ and the magnetic field $\mathbf{B}$.

electron velocity than the measured $\mathbf{V}_e$. We thus recalculate the electron heat flux $\mathbf{Q}_e^*$ with respect to $\mathbf{V}_p$ (equation (4)). The histogram of the difference between the azimuth of $\mathbf{Q}_e^*$ and the azimuth of $\mathbf{B}$ is also displayed for comparison in Figure 11a (dashed line): it peaks correctly at $180°$ and $360°$. This implies that $\mathbf{Q}_e^*$ is a better estimation of the electron heat flux than $\mathbf{Q}_e$.

Moreover, as $\mathbf{Q}_e$, $\mathbf{Q}_e^*$ has also been calculated with $E_{\min} = 9.65$ eV. We recall that over the period considered here, $e\phi/E_{\min}$ varies between 0 and 1 (see Figure 10a), so that a more or less important part of the core electrons is missing, which could affect the estimation of $\mathbf{Q}_e^*$. We have seen (section 3.2) that as a consequence of this effect, the ratio $N_{e\,\mathrm{df}}/N_{e\,\mathrm{TNR}}$ can be either smaller or larger than unity. Thus we display, in Figure 11b, a 2-D histogram of the values of $[Az(\mathbf{Q}_e^*) - Az(\mathbf{B}), N_{e\,\mathrm{df}}/N_{e\,\mathrm{TNR}}]$ as contours of isoprobability of occurrence, which shows that the direction of

$\mathbf{Q}_e^*$ does not depend on $N_{e\,\mathrm{df}}/N_{e\,\mathrm{TNR}}$ (or $e\phi/E_{\min}$). The same conclusion holds for the modulus of $\mathbf{Q}_e^*$, implying that neither its direction nor its amplitude depends on the fact that part of the core electrons is missing, whatever its proportion. This is in agreement with a total heat flux dominated by the halo electron particle flux, in the frame of the total electron distribution [Scime et al., 1994b].

The moduli of $\mathbf{Q}_e$ and of $\mathbf{Q}_e^*$ are displayed as functions of the cosine of the angle between the heat flux and the magnetic field, respectively, in Figure 12a and Figure 12b. These figures confirm that $\mathbf{Q}_e^*$ is closer to $\mathbf{B}$ than $\mathbf{Q}_e$ and show that the average of $|\mathbf{Q}_e^*|$ is ~ 2 times smaller than the average of $|\mathbf{Q}_e|$. The largest values of the heat flux found in our sample are 30 μW m^{-2}, but $|\mathbf{Q}_e^*|$ is generally below 10 μW m^{-2} (see Figure 12b). These values are consistent with those found by Pilipp et al. [1990] and Scime et al. [1994b] at 1 AU.

7. Summary and Conclusion

In this paper we have compared the solar wind electron parameters obtained on Wind simultaneously with the TNR wave receiver of the WAVES experiment and the electron electrostatic analyzers of the 3DP experiment. This is the first time that such a detailed comparison of simultaneous measurements made by a radio wave receiver and a particle instrument has been made, allowing a recalibration of the particle data.

The main results of this work can be summarized as follows:

1. The electron densities provided by both instruments are observed to be significantly different. We interpret these differences as due to the spacecraft charging effects coupled with the effects of the low-energy cutoff of the energy sweeping in the electron spectrometer, $E_{\min}$ (~ 10 eV).

2. We show that one can account very well for such differences through a simple physical model of the particle spectrometer, taking into account both the spacecraft charging effect and the low-energy cutoff in the energy sweeping. The model, valid for $e\phi < E_{\min}$, is based on the assumption that the solar wind electron distribution is a simple Maxwellian, and that the spacecraft potential ϕ modifies only the electron energies (the electron trajectories remaining unchanged) and affects the electron distributions isotropically. The main advantage of such a model is that it provides simple analytical relations for the measured electron density and temperature as functions of the "real" ones.

3. Because the spacecraft potential ϕ is unknown, as is often the case, we consider the TNR density to be the real electron density, in order to fix the parameters of the model and derive quasi-empirical relations for correcting the electron density and temperature. We show then that these quantities are very well corrected, to better than 5% for density and 10% for temperature. Moreover, the corrected 3DP electron temperature is in

very good agreement with that measured with TNR, to better than 10%. Finally, the model allows prediction of the value of the spacecraft potential ϕ. We show that it matches the expected values, so that the uncertainty on the measured electron moments is due to the low-energy cutoff and spacecraft charging rather than to the photoelectrons, $e\phi$ being always below $E_{\min}$.

4. Taking into account the conditions of charge neutrality and zero electric current in the solar wind, it is seen that the proton bulk velocity is a better approximation of the real electron bulk velocity than the measured one itself. So the electron heat flux is clearly improved when calculated in the frame of the proton velocity instead of the electron velocity. Indeed, its direction is found to be aligned with the magnetic field, while it was found 20° away from it when calculated in the electron frame.

This new method for correcting particle data is based on the use of simple, semiempirical relations; it is reliable and can be routinely used to determine accurate electron parameters at a rapid cadence.

In any case, in spite of the spacecraft charging and low-energy cutoff effects, the electron electrostatic analyzers remain an essential means to investigate the actual shape and the fine details of the electron distribution functions in the solar wind (and more generally in space plasmas). Although very different, thermal noise spectroscopy is complementary in measuring accurately the density and bulk electron temperature when spacecraft charging cannot be properly eliminated. Sophisticated methods with intrinsically complex spacecraft geometry for correcting fully for the effect of the corresponding potential on the ambient electrons are sometimes irrelevant. Frequently, such methods depend more and more on parameters that are poorly known and cannot be easily applied to a different case. By comparing simultaneous measurements on Ulysses, from the Solar Wind Observations Over the Poles of the Sun (SWOOPS) electron analyzer [Bame et al., 1992] and from the thermal noise spectroscopy with the URAP radio receiver [Stone et al., 1992], Maksimovic et al. [1995] have shown that the initial difference of 19% between the densities obtained from the two instruments is only reduced to 13% by using improved SWOOPS data obtained with the vectorial correction method of S/C charging effects [Scime et al., 1994a]. Our model, whose formulas were also validated, seems to contain the essence of the physics making it possible to explain how the electron measurements made by the electrostatic analyzers are altered. However, the exact parameters of the model depend on time, on the fatigue of the detectors (microchannel plates (MCPs)), and eventually on other instrumental effects related to particle analyzers. Fatigue of the detectors is partially corrected on board by periodically increasing the high voltage applied to the MCPs (in order to increase the gain). The exact value of the density is thus difficult to obtain by a particle spectrometer alone, improving

the utility of a thermal noise receiver from which the plasma frequency can be obtained without requiring a receiver gain calibration. We could thereafter improve the model described in this paper by taking into account the suprathermal electron population that have been neglected in this study and/or generalize it to the case of a drifting plasma (with a nonzero bulk velocity). Nevertheless, the equations of the model presented in this paper can already be applied to electron measurements on board other spacecrafts equipped with instruments for measuring the thermal noise, such as URAP [Stone et al., 1992] on Ulysses or RPWS [Gurnett et al., 2001] on Cassini.

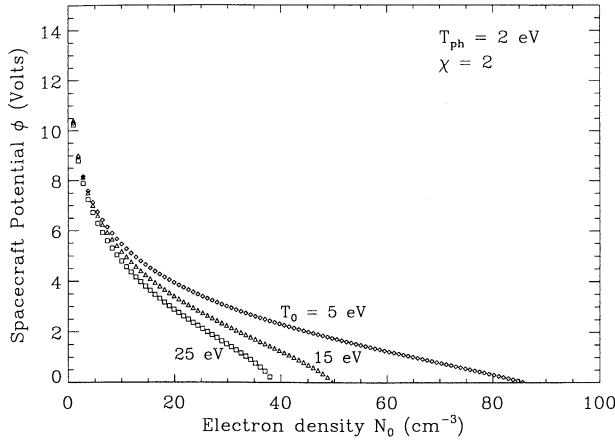## Appendix A: Spacecraft Electrical Potential

In most practical cases the charging of a body in space is due to a balance between some of the following physical processes: (1) ambient electrons and ions striking the surface of the body and transfering their charge; (2) incident energetic electrons striking the surface, inducing secondary emission of electrons; and (3) incident energetic photons inducing photoelectron emission.

When a surface is illuminated by a flux of ionizing radiation, it emits photoelectrons. The number of ejected photoelectrons per absorbed photon, $W(E)$, depends on the physical and chemical structure of the material. The photoemission flux is found by integrating over the spectrum the product of $W(E)$ by the absorbed solar flux $S(E)$ [see Grard, 1973]. Photoelectrons are ejected with a typical energy of 1-2 eV, which can be approximated by a temperature $k_B T_{ph} \sim$ 1-2 eV. The photoelectron saturation current density, J_{ph0}, is obtained simply by multiplying the photoemission flux by the elementary charge e. This leads to

$$J_{ph0} \approx \frac{10^{-5}\chi}{d_{AU}^2} \qquad (A1)$$

where the unit is A m^{-2}, χ is a parameter depending on the material of the spacecraft, and d_{AU} is the solar distance in astronomical units; $10^{-5}\chi$ is the photoelectron saturation current density at 1 AU, and χ is of the order of 2 [see Grard, 1973, Table 2]. J_{ph0} can vary from a few to several tens of μA m^{-2}; the photoelectron density is of the order of $10 - 10^3$ cm^{-3} in the vicinity of the spacecraft.

Suppose now that photoemission prevails, i.e., $J_{ph0} > J_{e0}$, J_{e0} being the unperturbed (for spacecraft potential $\phi = 0$) ambient electron current density, and that secondary emission is negligible, so that the charging is determined by a balance between collection of ambient electrons and emission of photoelectrons. This usually occurs in the interplanetary medium at Earth's orbit. As $m_e \ll m_i$ (where m_e and m_i are the electron and proton mass, respectively), the ambient proton current density can also be neglected.

Figure A1. Theoretical spacecraft electrical potential $\phi(N_{e0}, T_{e0})$ as a function of electron density N_{e0}, determined from a balance between collection of ambient electrons and emission of photoelectrons. It is obtained as a solution of equation (A7), for $T_{ph} = 2$ eV and $\chi = 2$. Here ϕ is plotted for three different temperatures, $T_{e0} = 5$, 15 and 25 eV.

Since photoemission prevails, the object charges positively, thereby attracting photoelectrons, so that only those emitted with an energy larger than $e\phi$ can escape. The photoelectron flux depends also on the geometry.

Let us assume, as a first approximation, that the spacecraft is a sphere with a radius r_s: in three dimensions the photoelectron flux is just the flux of those emitted with a kinetic energy larger than $e\phi$. Assuming that the photoelectrons have a Maxwellian energy distribution with a temperature T_{ph} and integrating over the relevant velocity space, one finds for $\phi > 0$ [see *Grard*, 1973]:

$$J_{ph} = J_{ph0}\left(1 + \frac{e\phi}{k_B T_{ph}}\right) e^{-e\phi/k_B T_{ph}}, \qquad (A2)$$

in A m^{-2}. The ambient electron current density is defined by

$$J_e = e\, N_e\, v_e, \qquad (A3)$$

where N_e and v_e are the electron density and velocity, respectively, at the surface of the spacecraft. We assume also that the ambient solar wind electrons have a Maxwellian distribution f with a density N_{e0} and a temperature T_{e0} and that the velocity distribution observed at the surface of the spacecraft is the one given by (15). If we assume isotropy, the electron velocity v_e at the surface of the spacecraft is then

$$v_e = \frac{4\pi}{N_e} \int_{v_\phi}^{\infty} v'\, f'(v')\, v'^2 dv', \qquad (A4)$$

where v_ϕ is given by (8). After integration, one finds [see e.g., *Garrett*, 1981]

$$J_e = J_{e0}\left(1 + \frac{e\phi}{kT_{e0}}\right), \qquad (A5)$$

where

$$J_{e0} = \frac{2e}{\sqrt{\pi}}\, N_{e0}\, v_{th}. \qquad (A6)$$

Normally, the floating potential of the spacecraft ϕ is defined by the equality between photocurrent $J_{ph}\, S_{ph}$ and plasma current $J_e\, S_e/4$, where S_{ph} and S_e are the photoelectron emission area (πr_s^2) and the electron collection area $(4\pi r_s^2)$, respectively; the factor $1/4$ for the ambient electrons arises because only $N_{e0}/2$ particles per unit volume are approching a given infinitesimal surface element from one side with an average perpendicular velocity $\langle v \rangle/2 = v_{th}/\sqrt{\pi}$.

In this way, by just writing $J_e = J_{ph}$, we obtain a nonlinear expression for the spacecraft potential

$$\frac{e\phi}{T_{ph}} - \ln\left[\frac{(1 + e\phi/T_{ph})}{(1 + e\phi/T_{e0})}\, \frac{96.15\,\chi}{N_{e0}\,\sqrt{T_{e0}}\, d_{AU}^2}\right] = 0, \qquad (A7)$$

where N_{e0} is given here in cm^{-3}, and T_{ph} and T_{e0} are in eV. In order to calculate the spacecraft potential ϕ, we compute the root of (A7) as a function of N_{e0} and T_{e0}, with $T_{ph} = 2$ eV, $\chi = 2$ and $d_{AU} = 1$ AU. The result is shown in Figure A1, where we display the spacecraft potential as a function of the electron density N_{e0}, for different values of the electron temperature T_{e0}: ϕ depends appreciably on the electron temperature only for solar wind densities above ~ 10 cm^{-3}. For solar wind densities above 40 to 50 cm^{-3}, the S/C potential seems to reach negative values, so that it cannot be determined by a simple balance between photoelectrons and ambient electrons, as the one considered here.

References

Bame, S. J., D. J. McComas, B. L. Barraclough, J. L. Phillips, K. J. Sofaly, J. C. Chavez, B. E. Goldstein, and R. K. Sakurai, The ULYSSES solar wind plasma experiment, *Astron. Astrophys. Suppl. Ser.*, *92*, 237–265, 1992.

Bougeret, J.-L., *et al.*, WAVES: The radio and plasma wave investigation on the WIND spacecraft, *Space Sci. Rev.*, *71*, 231–263, 1995.

Chateau, Y. F., and N. Meyer-Vernet, Electrostatic noise in non-Maxwellian plasmas: Generic properties and Kappa distributions, *J. Geophys. Res.*, *96*, 5825–5836, 1991.

Fazakerley, A. N., S. J. Schwartz, and G. Paschmann, Measurement of plasma velocity distributions, in *Analysis Methods for Multi-Spacecraft Data, ESA Publ. ISSI-SR-001*, edited by G. Paschmann and P. W. Daly, pp. 91–124, Int. Space Sci. Institute, Bern, Switzerland, 1998.

Feldman, W. C., J. R. Asbridge, S. J. Bame, M. D. Montgomery, and S. P. Gary, Solar wind electrons, *J. Geophys. Res.*, *80*, 4181–4196, 1975.

Garrett, H. B., The charging of spacecraft surfaces, *Rev. Geophys.*, *19*, 577–616, 1981.

Goertz, C. K., Dusty plasmas in the solar system, *Rev. Geophys.*, *27*, 271–292, 1989.

Grard, R. C. L., Properties of the satellite photoelectron sheath derived from photoemission laboratory measurements, *J. Geophys. Res.*, *78*, 2885–2906, 1973.

Gurnett, D. A., *et al.*, The Cassini radio and plasma wave investigation, *Space Sci. Rev.*, in press, 2001.

Issautier, K., N. Meyer-Vernet, M. Moncuquet, and S. Hoang, Solar wind radial and latitudinal structure: Electron density and core temperature from Ulysses thermal noise spectroscopy, *J. Geophys. Res.*, *103*, 1969–1979, 1998.

Issautier, K., N. Meyer-Vernet, M. Moncuquet, S. Hoang, and D. J. McComas, Quasi-thermal noise in a drifting plasma: Theory and application to solar wind diagnostic on Ulysses, *J. Geophys. Res.*, *104*, 6691–6704, 1999.

Lepping, R. P., *et al.*, The Wind magnetic field investigation, *Space Sci. Rev.*, *71*, 207–229, 1995.

Lin, R. P., *et al.*, A three-dimensional plasma and energetic particle investigation for the WIND spacecraft, *Space Sci. Rev.*, *71*, 125–153, 1995.

Maksimovic, M., S. Hoang, N. Meyer-Vernet, M. Moncuquet, J.-L. Bougeret, J. L. Phillips, and P. Canu, Solar wind electron parameters from quasi-thermal noise spectroscopy and comparison with other measurements on Ulysses, *J. Geophys. Res.*, *100*, 19,881–19,891, 1995.

Maksimovic, M., J.-L. Bougeret, C. Perche, J. T. Steinberg, A. J. Lazarus, A. F. Viñas, and R. J. Fitzenreiter, Solar wind density intercomparisons on the WIND spacecraft using WAVES and SWE experiments, *Geophys. Res. Lett.*, *25*, 1265–1268, 1998.

Meyer-Vernet, N., and C. Perche, Toolkit for antennae and thermal noise near the plasma frequency, *J. Geophys. Res.*, *94*, 2405–2415, 1989.

Meyer-Vernet, N., S. Hoang, K. Issautier, M. Maksimovic, R. Manning, M. Moncuquet, and R. G. Stone, Measuring plasma parameters with thermal noise spectroscopy, in *Measurements Techniques for Space Plasma: Fields, Geophys. Monogr. Ser.*, vol. 103, edited by R. F. Pfaff, J. E. Borovsky, and D. T. Young, pp. 205–210, AGU, Washington D.C., 1998.

Montgomery, M. D., S. J. Bame, and A. J. Hundhausen, Solar wind electrons: Vela 4 measurements, *J. Geophys. Res.*, *73*, 4999–5003, 1968.

Ogilvie, K. W., *et al.*, SWE, A comprehensive plasma instrument for the Wind spacecraft, *Space Sci. Rev.*, *71*, 55–77, 1995.

Paschmann, G., A. N. Fazakerley, and S. J. Schwartz, Moments of plasma velocity distributions, in *Analysis Methods for Multi-Spacecraft Data, ESA Publ. ISSI-SR-001*, edited by G. Paschmann and P. W. Daly, pp. 125–157, Int. Space Sci. Institute, Bern, Switzerland, 1998.

Paularena, K. I., and A. J. Lazarus, Comment on "Intercalibration of solar wind instruments during the international magnetospheric study" by S. M. Petrinec and C. T. Russell, *J. Geophys. Res.*, *99*, 14,777–14,778, 1994.

Petrinec, S. M., and C. T. Russell, Intercalibration of solar wind instruments during the international magnetospheric study, *J. Geophys. Res.*, *98*, 18,963–18,970, 1993.

Petrinec, S. M., and C. T. Russell, Reply, *J. Geophys. Res.*, *99*, 14,779–14,780, 1994.

Phillips, J. L., S. J. Bame, J. T. Gosling, D. J. McComas, B. E. Goldstein, and A. Balogh, Solar wind thermal electrons from 1.15 to 5.34 AU: Ulysses observations, *Adv. Space Res.*, *13*(6), 47–50, 1993.

Pilipp, W. G., H. Miggenrieder, M. D. Montgomery, K.-H. Mülhaüser, H. Rosenbauer, and R. Schwenn, Characteristics of electron velocity distribution functions in the solar wind derived from the Helios Plasma Experiment, *J. Geophys. Res.*, *92*, 1075–1092, 1987.

Pilipp, W.G., H. Miggenrieder, K.-H. Mülhaüser, H. Rosenbauer, and R. Schwenn, Large-scale variations of thermal electron parameters in the solar wind between 0.3 and 1 AU, *J. Geophys. Res.*, *95*, 6305–6329, 1990.

Richaume, P., Approche connexionniste pour le pilotage temps réel du récepteur numérique WAVES/TNR embarqué sur la sonde spatiale WIND, Ph.D. dissertation, DESPA, Paris Observatory, Paris, France, 1996.

Rosenbauer, H., R. Schween, E. Marsch, B. Meyer, H. Miggenrieder, M. D. Montgomery, K.-H. Mülhaüser, W. G. Pilipp, W. Voges, and S. M. Zink, A survey on initial results of the Helios Plasma experiment, *J. Geophys.*, *42*, 561–580, 1977.

Russell, C. T., and S. M. Petrinec, On the relative intercalibration of the solar wind instruments on IMP-8 and ISEE-3, *Geophys. Res. Lett.*, *19*, 961–963, 1992.

Scime, E. E., J. L. Phillips, and S. J. Bame, Effects of spacecraft potential on three-dimensionnal electron measurements in the solar wind, *J. Geophys. Res.*, *99*, 14,769–14,776, 1994a.

Scime, E. E., S. J. Bame, W. C. Feldman, S. P. Gary, J. L. Phillips, and A. Balogh, Regulation of the solar wind electron heat flux from 1 to 5 AU: Ulysses observations, *J. Geophys. Res.*, *99*, 23,401–23,410, 1994b.

Scudder, J. D., E. C. Sittler, and H. S. Bridge, A survey of the plasma electron environment of Jupiter: A view from Voyager, *J. Geophys. Res.*, *86*, 8157–8179, 1981.

Song, P., X. X. Zhang, and G. Paschmann, Uncertainties in plasma measurements: Effects of lower cutoff energy and spacecraft charge, *Planet. Space Sci.*, *45*, 255–267, 1997.

Stone, R. G., J.-L. Bougeret, J. Caldwell, P. Canu, Y. De Conchy, N. Cornilleau-Wehrlin, M. D. Desch, G. J. Fainberg, K. Goetz, and M. L. Goldstein, The Unified Radio and Plasma Wave Investigation, *Astron. Astrophys. Suppl. Ser.*, *92*, 291–316, 1992.

Whipple, E. C., Potentials of surfaces in space, *Rep. Prog. Phys.*, *44*, 1197–1250, 1981.

Jean-Michel Bosqued, Centre d'Etude Spatiale des Rayonnements, Université Paul Sabatier, B.P. 4346, Toulouse, France.

Jean-Louis Bougeret, Milan Maksimovic, André Mangeney, and Claude Perche, Département de Recherche Spatiale, CNRS UMR-8632, Observatoire de Paris-Meudon, 92195 Meudon Cedex, France.

Davin E. Larson, Robert P. Lin, and Chadi Salem, Space Sciences Laboratory, University of California, Berkeley, CA 94720-7450, USA (email: salem@ssl.berkeley.edu).